catalysts

MDPI

Article

The Impact of Polymerization Atmosphere on the Microstructure and Photocatalytic Properties of Fe-Doped g-C_3N_4 Nanosheets

Xiaoyu Peng, Xiufang Chen *, Rui Pang, Lanlan Cheng, Fengtao Chen and Wangyang Lu

National & Local Joint Engineering Research Center for Textile Fiber Materials and Processing Technology, College of Material Science and Engineering, Zhejiang Sci-Tech University, Hangzhou 310018, China; xiaoyu__peng@163.com (X.P.); 19857115160@163.com (R.P.); cll73739703@163.com (L.C.); cft0923@163.com (F.C.); luwy@zstu.edu.cn (W.L.)

* Correspondence: chenxf@zstu.edu.cn

Abstract: Peroxymonosulfate (PMS, SO_5^{2-})-based oxidation is an efficient pathway for degrading organic pollutants, but it still suffers from slow degradation efficiency and low PMS utilization. In this work, we report the preparation of porous Fe-doped g-C_3N_4 catalysts by one-step thermal polymerization using urea and transition metal salts as precursors and investigate the effect of atmosphere conditions (air and nitrogen) on the catalytic performance. Systematic characterizations show that Fe-doped g-C_3N_4 prepared in air (FeN_x-CNO) has a larger specific surface area (136.2 $m^2\ g^{-1}$) and more oxygen vacancies than that prepared in N_2 (FeN_x-CNN, 74.2 $m^2\ g^{-1}$), giving it more active sites to participate in the reaction. Meanwhile, FeN_x-CNO inhibits the recombination of photogenerated carriers and improves the light utilization. The redox cycling of Fe(III) and Fe(II) species in the photocatalytic system ensures the continuous generation of $SO_5\bullet^-$ and $SO_4\bullet^-$. Therefore, FeN_x-CNO can remove CBZ up to 96% within 20 min, which is 3.4 times higher than that of CNO and 3.1 times higher than that of FeN_x-CNN, and the degradation efficiency can still retain 93% after 10 cycles of reaction. This study provides an economical and efficient method for photocatalysis in the degradation of medicines in contaminated water.

Keywords: Fe doping; graphitic carbon nitride; atmospheric effects; PMS activation; photocatalysis

check for updates

Citation: Peng, X.; Chen, X.; Pang, R.; Cheng, L.; Chen, F.; Lu, W. The Impact of Polymerization Atmosphere on the Microstructure and Photocatalytic Properties of Fe-Doped g-C_3N_4 Nanosheets. *Catalysts* **2024**, *14*, 520. https://doi.org/10.3390/catal14080520

Academic Editors: Panagiotis Dallas and Christos Trapalis

Received: 13 July 2024
Revised: 8 August 2024
Accepted: 9 August 2024
Published: 11 August 2024

1. Introduction

The rapid development of industrialization has led to the discharge of various pollutants into the water [1–3]. Apart from everyday garbage, industrial wastewater, and dyes, many types of medicine have been abused and discharged into water bodies in large quantities, causing serious contamination of water sources [4,5]. Even low-concentration pharmaceutical products and personal care products (PPCPs)—like carbamazepine (CBZ)—in the environment cause chronic and cumulative ecotoxicity to aquatic ecosystems and their biological populations and continue to pose a threat to human health and safety [6,7]. It is difficult to effectively and completely remove low-concentration pharmaceuticals in water by traditional wastewater treatment technologies. Thus, there is an urgent need to promote the development of wastewater treatment technology to eliminate pharmaceutical pollution [8]. In recent years, because of the inherent merits, including green, convenient operation and mild reaction conditions, photocatalytic oxidation technology has attained a promising potential in wastewater treatment for its ability to effectively degrade low-concentration pharmaceuticals into small compounds or CO_2 and H_2O [9–11]. Nevertheless, this single technology still suffers from the shortcoming of low efficiency, thus restricting its industrial applications. It has been proven that when photocatalysis and persulfate-based advanced oxidation processes were employed simultaneously, the degradation efficiency could be boosted by generating a variety of reactive oxygen species (ROS) by activating peroxymonosulfate (PMS) with catalysts [12–14]. The development of

non-toxic, effective, and stable photocatalytic materials is the key to realizing the industrial application of this technology [15].

Graphitized carbon nitride (g-C_3N_4), as a semiconducting polymer material, has captured the attention of researchers in photocatalytic field, owing to its visible-light response, good photochemical reactivity, as well as good stability [16,17]. Meanwhile, g-C_3N_4 can offer abundant N-anchoring sites with a lone pair of electrons to coordinate with metal elements to form a M-N_x structure, thus forming stable dispersed metal active sites [18,19]. However, the photocatalytic performance of g-C_3N_4 is not satisfactory owing to the rapid recombination of photogenerated carriers, which hinders its further application to some extent [15,20]. Many methods, including structural modification, elemental doping, construction of Z-scheme heterojunctions, and noble metal deposition, have been employed to modify g-C_3N_4 to improve its photocatalytic activity [18,21]. Among them, doping transition metal ions into the g-C_3N_4 polymeric network not only ameliorates the carrier lifetime and mobility of g-C_3N_4, but also narrows its band gap [22,23]. Iron is the most abundant transition metal element in the earth's crust and is regarded as a high-quality choice to modify g-C_3N_4 due to its high activity, low cost, and environmental friendliness [24]. It was reported that Fe doping into g-C_3N_4 could strengthen the PMS activating ability to generate more reactive radicals (e.g., $SO_4\bullet^-$, ·OH, $O_2\bullet^-$, $^1O_2$), and thus enhance its overall photocatalytic efficiency [25].

The structure and photocatalytic performance of Fe-doped g-C_3N_4 was strongly affected by the g-C_3N_4 precursors [26]. Dicyandiamide and melamine are most frequently used as the precursors to produce Fe-doped g-C_3N_4 by thermal polymerization under inert atmosphere [27]. Iron ions can be entrapped in a high loading level by pyridinic nitrogen groups within the cavities of the heptazine rings in g-C_3N_4. Yet, nonporous Fe-doped g-C_3N_4 with a low surface area (< 20 m^2 g^{-1}) and limited active sites was yielded by this preparation method, which is not conducive to metal atom utilization and its photocatalytic reaction. Chemical etching with acid is needed to post-treat the as-prepared Fe-doped g-C_3N_4 to obtain a Fe catalyst with ultra-small size clusters or atomically dispersed metal species [28–30]. Recently, urea was found to be superior precursor for the fabrication of Fe-doped g-C_3N_4 nanosheets with a porous structure, which had a higher surface area and improved photocatalytic activity than Fe catalyst prepared by either dicyandiamide or melamine [31,32].

A few studies have revealed that polymerization atmosphere can affect the defects and the generation of carbon and nitrogen vacancies, thus altering the chemical structure and catalytic properties of carbon nitride [33,34]. For instance, Jiménez-Calvo et al. [35] enhanced H_2 production from water under solar and visible light irradiation by varying the g-C_3N_4 synthesis atmosphere (air, N_2, H_2, Ar, and NH_3). Guo and coworkers [36] reported that the posttreatment of bulk g-C_3N_4 under NH_3 atmosphere could result in the formation of abundant in-plane holes, thus obtaining holy g-C_3N_4 nanosheets. However, it is unclear that how the polymerization atmospheres can affect the physicochemical properties of Fe-doped g-C_3N_4 prepared from urea. Investigation on the effect of polymerization atmospheres on the catalytic activity of Fe-doped g-C_3N_4 for pharmaceutical elimination is scarce yet highly desirable. In this work, we developed an effective and stable porous Fe-doped carbon nitride catalyst containing highly dispersed Fe-N_x active sites by one-step thermal polymerization of the mixture of urea and Fe-containing salts in air and nitrogen conditions. Their catalytic performance for CBZ elimination was comprehensively investigated using PMS as the oxidant and simulate sunlight as light source. The effect of polymerization atmospheres on the chemical structure, textural and optical properties, as well as photocatalytic activity of Fe-doped g-C_3N_4 were studied in detail. It was found that the photocatalytic properties of Fe-doped g-C_3N_4 prepared from urea were strongly impacted by different polymerization atmospheres. FeN_x-CNO prepared in air had much higher photocatalytic activity than FeN_x-CNN prepared in nitrogen gas, and its degradation efficiency for CBZ was 3.1 times higher than that of FeN_x-CNN. A

possible pathway for CBZ degradation by the FeN_x-CNO/PMS photocatalytic system was also proposed.

2. Results and Discussion

2.1. Fabrication Process of FeN_x-CN Photocatalysts

The Fe-doped g-C_3N_4 catalyst was synthesized in situ by one-step thermal polymerization, and the preparation route is shown in Scheme 1. First, urea was fully mixed with ferric nitrate in aqueous solution, which was then dried at 80 °C to remove water and form a Fe–urea complex. Then, the mixture was placed in a semi-closed alumina crucible with a cover, and pyrolyzed at 550 °C in static air or N_2 atmosphere. During this procedure, the Fe–urea complex was polymerized to graphitic carbon nitride, and Fe species were immobilized into a g-C_3N_4 matrix by forming a Fe-N_x structure simultaneously. At the same time, abundant gases (e.g., NH_3, NO, CO) were produced, leading to an apparent volume expansion. Consequently, porous Fe-doped carbon nitride nanosheets were yielded. In this process, air or N_2 was used as the reaction atmosphere, denoted as n%FeN_x-CNO and n%FeN_x-CNN, respectively. n% (0.5%, 1%, 2%, and 3%) is the mass fraction of the initial mass of Fe to the total mass of FeN_x-CN catalyst.

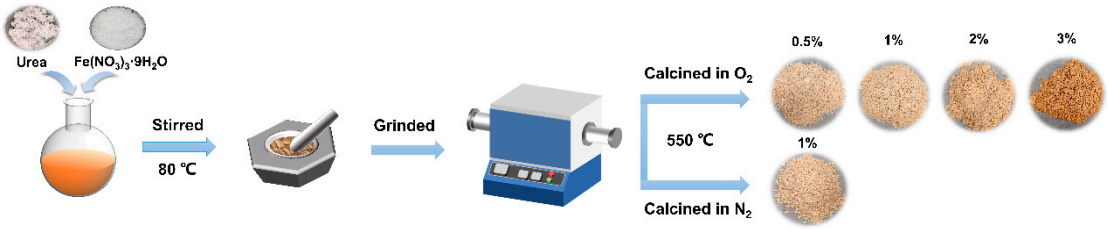

Scheme 1. Schematic sketch of the FeN_x-CN photocatalyst synthesis process.

2.2. Characterizations of FeN_x-CN Catalysts

In order to study the change in crystalline and chemical structure in various catalysts, the CNO and n%FeN_x-CNO were characterized by XRD and FT-IR, with those of CNN and 1%FeN_x-CNN as a comparison. Figure S1a shows the XRD patterns of FeN_x-CNO with Fe content varying from 0% to 3%. All patterns display two peaks at around 13.2° and 27.4°, indexed to (100) plane and (002) plane. They are attributable to the periodic arrangement of the layered tri-s-triazine ring structural units of g-C_3N_4 and the interlayer stacking of the conjugated aromatic rings, respectively [37,38]. The results prove that Fe doping does not change the main structure of carbon nitride. Compared to CNO, the intensity of (002) peak in the FeN_x-CNO with different Fe content was weakened, probably due to the incomplete polymerization of the graphitic layer and the disruption of stacking degree within the g-C_3N_4 structure caused by Fe doping [39]. Interestingly, no obvious peaks belonging to metallic Fe or iron oxides were found in the FeN_x-CNO with different Fe content, which implies that Fe might be incorporated into the carbon nitride framework by forming Fe-N_x coordination. The XRD patterns of CNO, 1%FeN_x-CNO and CNN, and 1%FeN_x-CNN are also compared in Figure 1a. Compared with CNO and 1%FeN_x-CNO prepared in air, the intensities of the characteristic diffraction peaks of CNN and 1%FeN_x-CNN catalysts were significantly enhanced, suggesting that the nitrogen atmosphere helps improve the regular stacking of the aromatic rings, thus resulting in an enhanced crystallization degree.

Figure S1b shows the FT-IR spectra of the CNO and n%FeN_x-CNO catalysts, which showed primary absorption bands at 2800–3500 cm^{-1}, 1200–1650 cm^{-1}, and 812 cm^{-1}. The results prove that N–H/O–H, C=N bonds in the aromatic ring, and the tri-s-triazine ring structural unit in g-C_3N_4 were generated in these CN-based samples, and Fe doping did not disrupt the basic bonding structure of carbon nitride [40,41]. As shown in Figure 1b, compared with those of CNO and FeN_x-CNO, the characteristic bands of CNN and FeN_x-CNN did not change significantly. It was found that FeN_x-CNN has higher intensity of the

characteristic peaks than FeN_x-CNO, implying the presence of more N-containing groups in the catalyst framework.

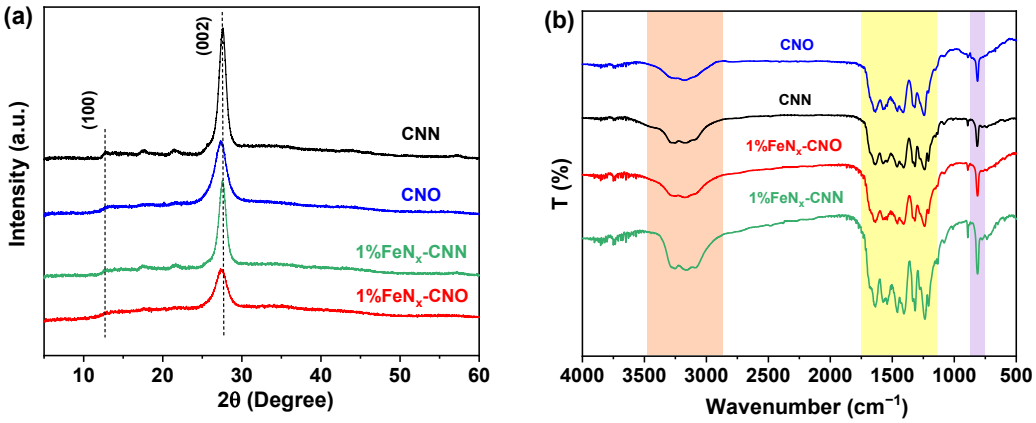

Figure 1. (**a**) XRD pattern and (**b**) FT-IR spectra of different catalysts.

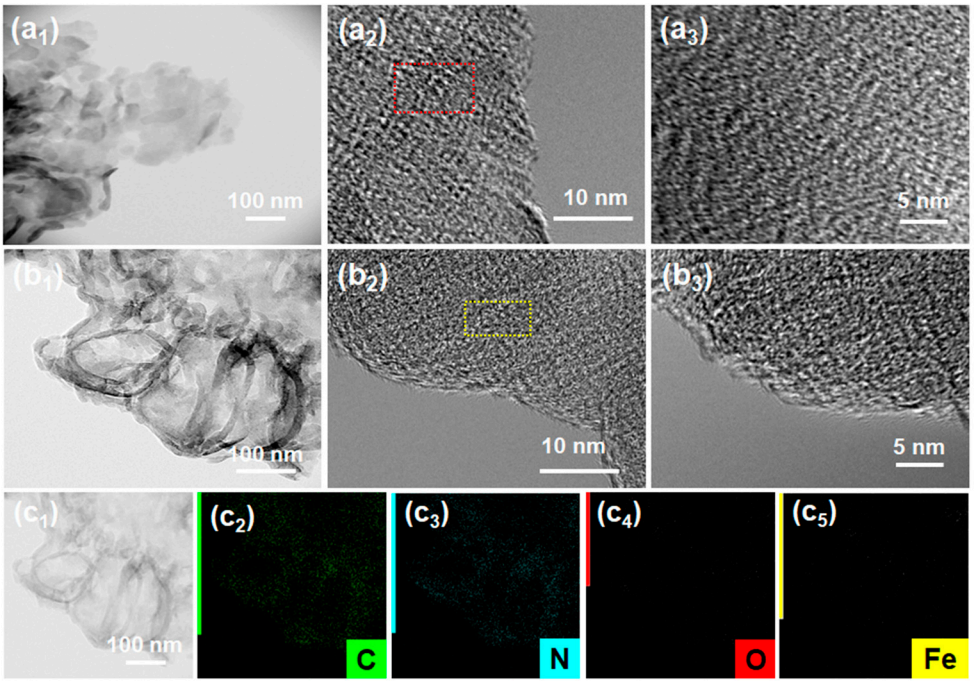

Figure 2. TEM and HRTEM images of (**a1**–**a3**) 1%FeN_x-CNN, (**b1**–**b3**) 1%FeN_x-CNO, and (**c1**–**c5**) STEM mapping images of 1%FeN_x-CNO.

The surface morphology and structural features of bulk 1%FeN_x-CN, 1%FeN_x-CNO, and 1%FeN_x-CNN were investigated using SEM. As shown in Figure S2a,b, bulk 1%FeNx-CN, prepared by dicyandiamide as precursor, exhibits dense structure without pores. From Figure S2c,d and Figure S2e,f, it can be observed that both 1% FeN_x-CNO and 1%FeN_x-CNN display a porous folded nanosheet stacking morphology with high porosity, which implies that the surface of 1%FeN_x-CNO and 1%FeN_x-CNN can provide a large number of reactive sites for adsorbing reactants and promoting carrier migration [42,43]. However, no visible large particles were found on the carbon nitride nanosheets, implying the incorporation of Fe into carbon nitride framework. The morphology of the CN-based catalysts was further observed by TEM images. Figure S3a–c displays the TEM images of CNO, which showed stacked large nanosheets with abundant pore structure. From Figure 2(a1), it can be seen that 1%FeN_x-CNN is mainly composed of smaller stacked nanosheet structure. As can be seen from Figure 2(b1), 1%FeN_x-CNO displayed stacking helical lamellae. HRTEM results

show that the many black dots were highly dispersed on the surface of 1%FeN_x-CNN and 1%FeN_x-CNO catalysts, and no crystalline phases appeared, suggesting that Fe may be embedded into the g-C_3N_4 organic framework (Figure 2(a3,b3)). STEM mapping images (Figure 2(c1)–(c4)) confirmed that the C, N, O, and Fe elements were uniformly distributed on g-C_3N_4.

In order to study the textural properties of the CN-based samples, the pore structure was further analyzed using a N_2 sorption measurement. As shown in Figure S4a, all three catalysts presented a type IV isothermal curve with H_3-type hysteresis loop [44]. The BJH pore size distribution in Figure S4b shows that the g-C_3N_4, 1%FeN_x-CNO, and 1%FeN_x-CNN pore sizes are mainly distributed around 25 nm, indicating mesoporous structure characteristics. The specific surface area, pore volume and average pore size of the catalysts are summarized in Table S1. Compared with pure g-C_3N_4 (66.3 m^2 g^{-1}), 1%FeN_x-CNN has a slightly higher specific surface area (74.2 m^2 g^{-1}), while 1%FeN_x-CNO (136.2 m^2 g^{-1}) has more than twice the specific surface area of g-C_3N_4. Meanwhile, the pore volumes of the catalysts were 1%FeN_x-CNO (0.874 cm^3 g^{-1}) > 1%FeN_x-CNN (0.688 cm^3 g^{-1}) > g-C_3N_4 (0.393 cm^3 g^{-1}). The above results suggest that Fe doping will induce disruption on the thermal polymerization process of urea, leading to changes in the surface charge of the graphitic plane, and reduced surface repulsion and lateral size of the graphitic plane. Thus, it can promote the formation of smaller nanosheets and more porous structure in both air and N_2 conditions. When Fe-doped g-C_3N_4 was prepared in air, the thermal polymerization process of urea was disrupted more severely, and more gases were generated than those in N_2 conditions, leading to a significant increase in the specific surface area of 1%FeNx-CNO. Compared to 1%FeN_x-CNN, 1%FeN_x-CNO has a larger specific surface area and abundant pores, which can expose more active sites, as well as promote the diffusion and transport of reactants from the aqueous phase to the inner and outer surfaces of the catalysts to participate in the photocatalytic reaction [45].

The surface elemental composition and chemical states of the catalysts were investigated using XPS. Figure S5 shows the XPS full spectra of CN and 1%FeN_x-CN. There are C, N, and O peaks in the XPS spectra of all the samples, except for a weak Fe peak in the spectrum of 1%FeN_x-CNO and 1%FeN_x-CNN. As shown in Figure 3a, the XPS C 1s spectra of CN and FeN_x-CN samples contain three peaks at 284.8, 286.3, and 288.2 eV, corresponding to graphitic carbon (C–C), sp3 C (C–NH_x), and a tri-s-triazine ring structural unit in the aryl ring (N=C–N), respectively. Compared to CN, the binding energies of the three peaks in the Fe-doped CN did not change after Fe doping, indicating that Fe was not coordinated with C in the g-C_3N_4. It has been reported in the literature that the defective C–C groups are related to the redox nature of the g-C_3N_4 surface [46]. As can be seen from Table S2, the percentage of defective C–C bonds increased from 12.8% (CNO) and 11.5% (CNN) to 28.8% (1%FeN_x-CNO) and 18.3% (1%FeN_x-CNN), respectively. This may be related to the inhibition of thermal polymerization of urea by Fe modification, which disrupts the two-dimensional periodic regular arrangement of the heptazine ring. The more irregular arrangement of the structural units of 1%FeN_x-CNO than 1%FeN_x-CNN indicates lower crystallization properties, which is also consistent with the previous XRD and FT-IR results. Figure 3b shows N 1s spectra of CNO, CNN, 1%FeN_x-CNO, and 1%FeN_x-CNN, which all had three peaks at around 398.6, 400.0, and 401.1 eV. These peaks correspond to the sp2 N (C–N=C) group, N–$(C)_3$ group, and terminal amino group (C–NH_x) of the tri-s-triazine ring, respectively. It is noteworthy that there is no change in the N peaks of CNO and CNN. In contrast, the C–N=C peaks in both 1%FeN_x-CNO and 1%FeN_x-CNN were shifted by 0.1 eV towards higher binding energy. This may be caused by the formation of Fe-N ligand bonds by lone pairs of electrons in pyridine N [47,48].

The O 1s spectra In the Figure 3c show that oxygen In CNO mainly exists In the form of surface hydroxyl oxygen (O_s, 532.7 eV) and oxygen vacancies (O_v, 531.6 eV) [49], and Fe doping changes the charge environment near the O atoms. Both peaks shifted towards high binding energy by 0.1 eV. It is known that oxygen vacancy defects can promote the charge transfer. As shown in Table S3, the proportion of oxygen vacancy in FeN_x-CNO

(48.3%) was higher than in CNO (31.1%) and 1%FeN_x-CNN (40.7%). This suggests that 1%FeN_x-CNO may have a higher carrier transfer efficiency than that 1%FeN_x-CNN.

As shown in Figure 3d, Fe 2p in 1%FeN_x-CNO and 1%FeN_x-CNN can be divided into four peaks. The two peaks at 710.5 and 723.7 eV were associated with Fe(III), and the other two peaks at 715.3 and 728.5 eV were attributed to Fe(II) [50–52]. The percentages of Fe(III) in 1%FeN_x-CNO and 1%FeN_x-CNN were 65% and 55.1%, respectively. In addition, no peak related to metallic Fe was found, implying that Fe may be embedded in g-C_3N_4 through coordination with pyridine N atoms.

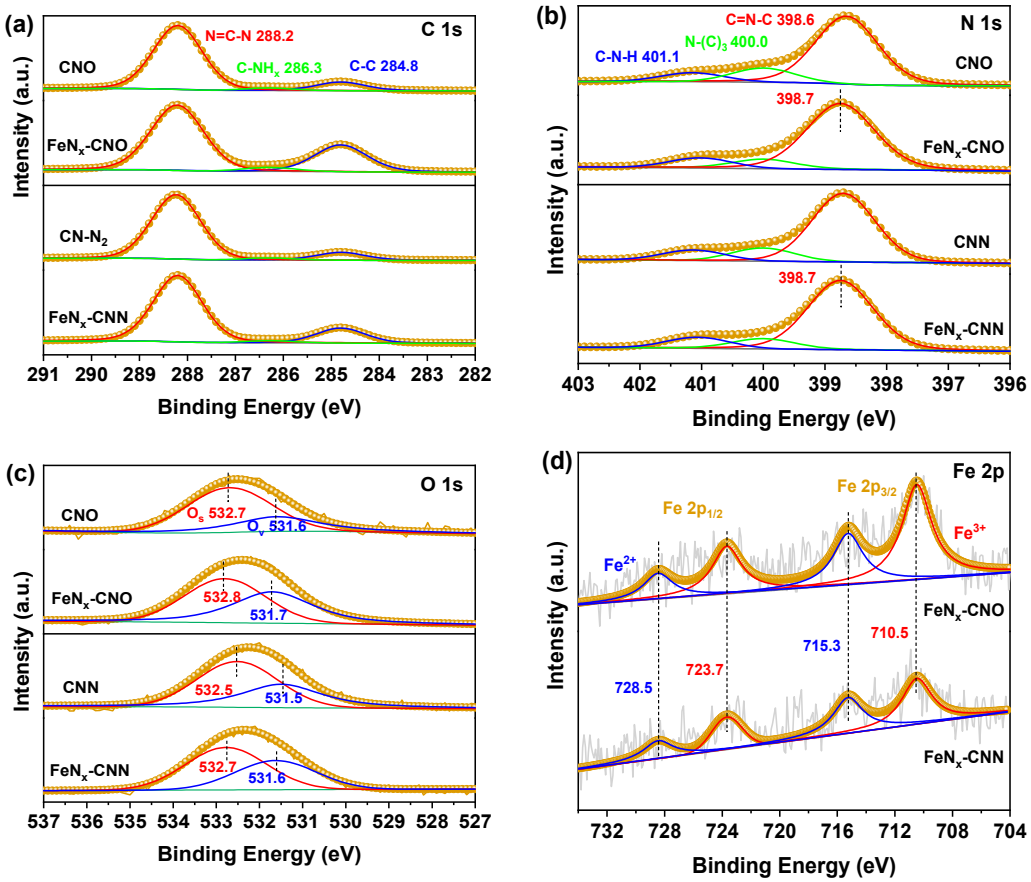

Figure 3. XPS spectra of CNO, CNN, 1%FeN_x-CNO, and 1%FeN_x-CNN. (**a**) C 1s, (**b**) N 1s, (**c**) O 1s, and (**d**) Fe 2p high-resolution XPS spectra.

The impact of polymerization atmospheres on the optical adsorption properties of Fe-doped g-C_3N_4 were investigated by UV–vis diffuse reflectance spectroscopy (DRS). As shown in Figure 4a, all the samples have light absorption in the range of 250–700 nm. CNO shows an absorption band edge at 460 nm, and a blue shift was observed in CNN. Fe modification results in the enhanced light absorption intensity in the region of at 250–400 nm and 450–700 nm, thus improving the light harvesting efficiency of both CNO and CNN. The result demonstrates that the formation of Fe-N_x bonds expands the visible light absorption capacity [53,54]. Compared to FeN_x-CNN, a slight red shift in the absorption band edge was found in FeN_x-CNO. As shown in Figure 4b, according to the Tauc equation, the band gaps (E_g) of CNO, CNN, 1%FeN_x-CNO, and 1%FeN_x-CNN are 2.82, 2.92, 2.78, and 2.89 eV, respectively. The valence band (VB) values of the above catalysts can be obtained from the XPS valence band spectra (Figure 4c), and their conduction band (CB) values can be obtained from the relationship between the energy bands. Figure 4d illustrates the band gap structures of CNO, CNN, 1%FeN_x-CNO, and 1%FeN_x-CNN. Since the redox potentials of $O_2/O_2\bullet^-$ and $OH^-/\bullet OH$ are −0.33 and 1.99 eV, respectively, the catalysts can be photoinduced to produce $O_2\bullet^-$ and •OH. The above results show that Fe doping

helps to improve the optical properties of the catalysts, and the 1%FeN_x-CNO synthesized under air requires less energy for electronic transition, while it is easier to diffuse carriers along the interface, which is more favorable for the photocatalytic reaction [55].

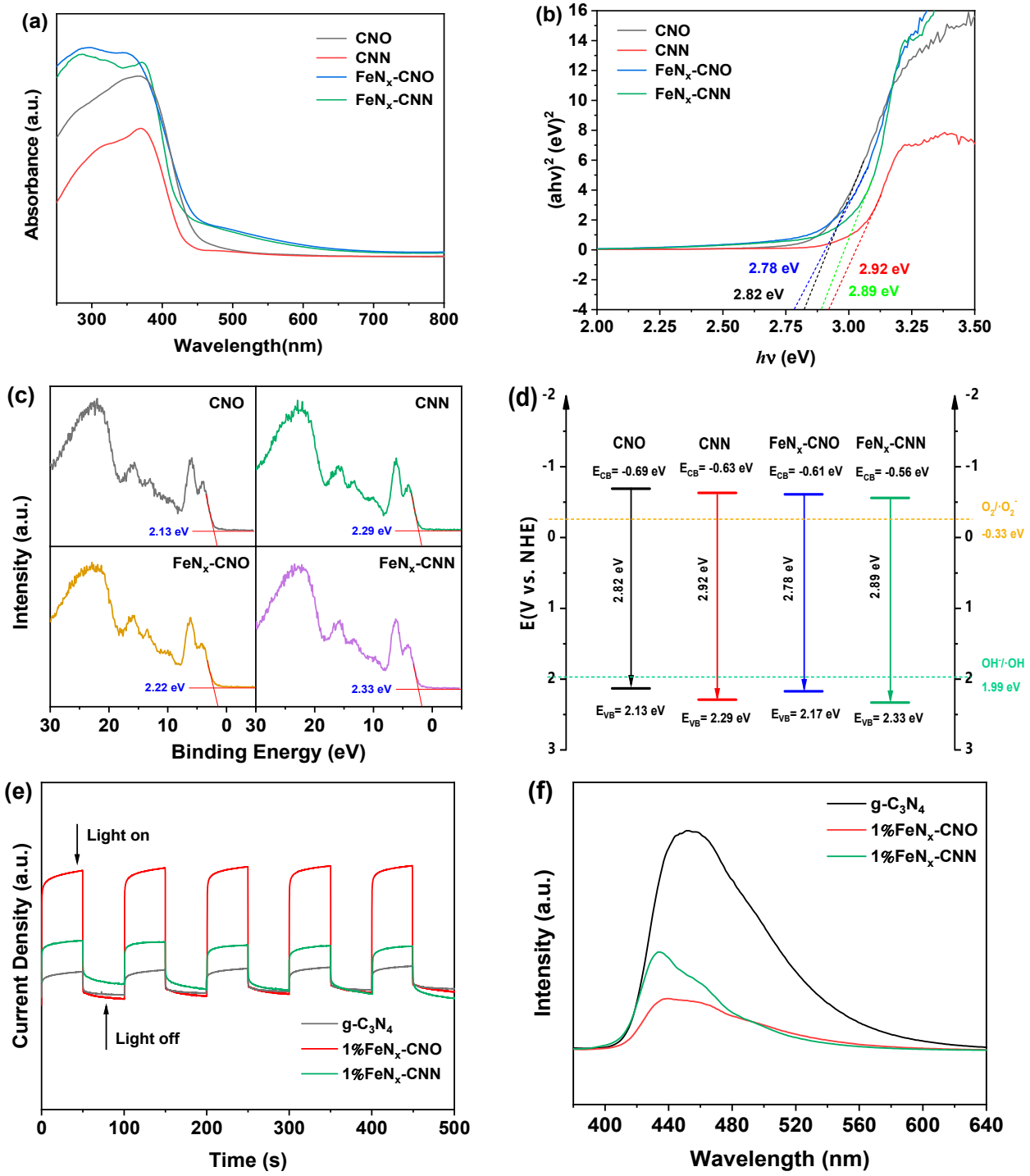

Figure 4. (**a**) Ultraviolet–visible diffuse reflection spectrum; (**b**) Tauc curve; (**c**) XPS valence band; (**d**) scheme of band gap structures for CNO, CNN, 1%FeN_x-CNO, and 1%FeN_x-CNN; (**e**) TPC response; and (**f**) PL spectrum of g-C_3N_4, 1%FeN_x-CNO, and 1%FeN_x-CNN.

Transient photocurrent (TPC) and fluorescence spectroscopy (PL) were also used to probe the photogenerated electron–hole separation transfer behaviors of g-C_3N_4, 1%FeN_x-CNO, and 1%FeN_x-CNN. Figure 4e shows that the photocurrent density response of

1%FeN_x-CNO was 4 and 2.3 times higher than that of g-C_3N_4 and 1%FeN_x-CNN, respectively, which indicated that 1%FeN_x-CNO could effectively promote the rapid separation of charge carriers. The interaction of N and Fe atoms in the form of Fe-N_x bonds might boost the e^-/h^+ separation efficiency and charge transfer rate. Moreover, the larger specific surface area of FeN_x-CNO provides more active sites in contact with the reactants and transfers them through interconnected transport channels in the catalyst [56].

Figure 4f shows the PL spectra of g-C_3N_4, 1%FeN_x-CNO, and 1%FeN_x-CNN under the excitation wavelength of 350 nm. Pure g-C_3N_4, 1%FeN_x-CNO, and 1%FeN_x-CNN all have strong and broad PL emission spectra at 400–600 nm. Among them, pure g-C_3N_4 has a strong PL peak centered at 450 nm. As a comparison, the intensity of the PL peak in the 1%FeN_x-CNO and 1%FeN_x-CNN was significantly weakened, which proved that Fe modification could effectively inhibit photogenerated carrier recombination efficiency. The emission peak intensity of 1%FeN_x-CNO was weaker than that of 1%FeN_x-CNN, which further proved that FeN_x-CNO was more effective in suppressing the recombination of photoexcitons, thus boosting the photocatalytic capability. In addition, it was observed that the emission peaks of 1%FeN_x-CNO and 1%FeN_x-CNN were blue-shifted to around 440 nm, which was caused by the decreased the bandgap energy by Fe incorporation. This is consistent with the DRS analysis [57].

2.3. Photocatalytic Performance Evaluation

The catalytic performance of various catalysts was studied by the photocatalytic degradation of CBZ under simulated sunlight irradiation. Figure 5a shows the effect of Fe dopant on the photocatalytic activity of CNO-based catalyst with PMS as oxidant. Fe doping was found to be effective in enhancing the photocatalytic degradation ability. Among them, 1%FeN_x-CNO had the highest efficiency in degrading CBZ, with a removal rate of up to 96% within 20 min. The reaction rate constant (k, 0.1542 min^{-1}) of 1%FeN_x-CNO was 3.4 times that of CNO (0.0425 min^{-1}) (Figure 5b). When the Fe content was higher than 1%, the photocatalytic activity of FeN_x-CNO reduced. A possible reason is that the high Fe doping might disrupt the thermal polymerization process of urea severely, and produce excessive defects, thus adverse to the photocatalytic reaction. So, the Fe doping amount of 1% was selected in the subsequent work. Figure 5c,d shows the influence of polymerization atmospheres on the catalytic activity of Fe-doped g-C_3N_4. The photocatalytic degradation efficiency with 1%FeN_x-CNO (96%) was much higher than that of 1%FeN_x-CNN (63%) within 20 min, and the k value was 3.1 times that of the 1%FeN_x-CNN catalyst. The result indicated that polymerization atmospheres had a great impact on the catalytic properties of Fe-doped g-C_3N_4. It is also worthy to note that 1%FeN_x-CNO had higher photocatalytic performance than that of most other types of catalysts for CBZ degradation in the presence of PMS (Table S4). The porous structure with a larger surface area and more defect sites (e.g., oxygen vacancy) formed during the polycondensation process of urea in air contributed to the higher catalytic activity of FeN_x-CNO.

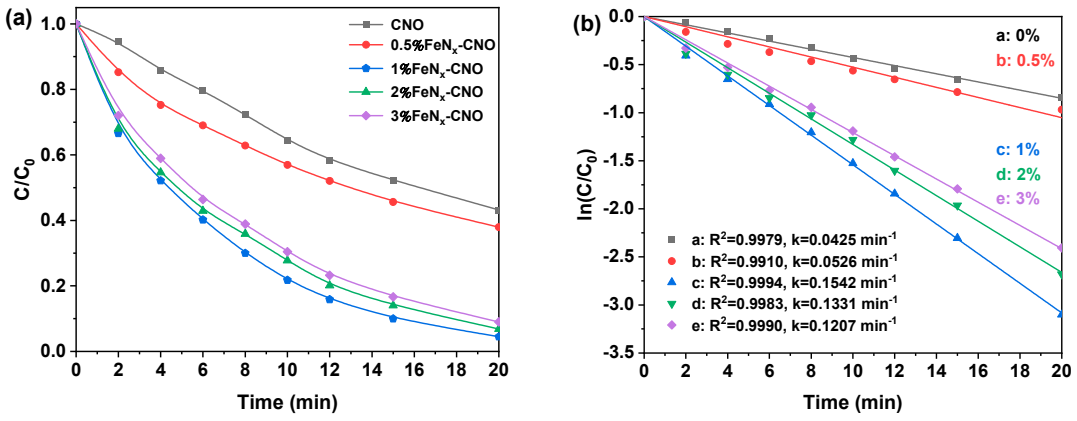

Figure 5. *Cont.*

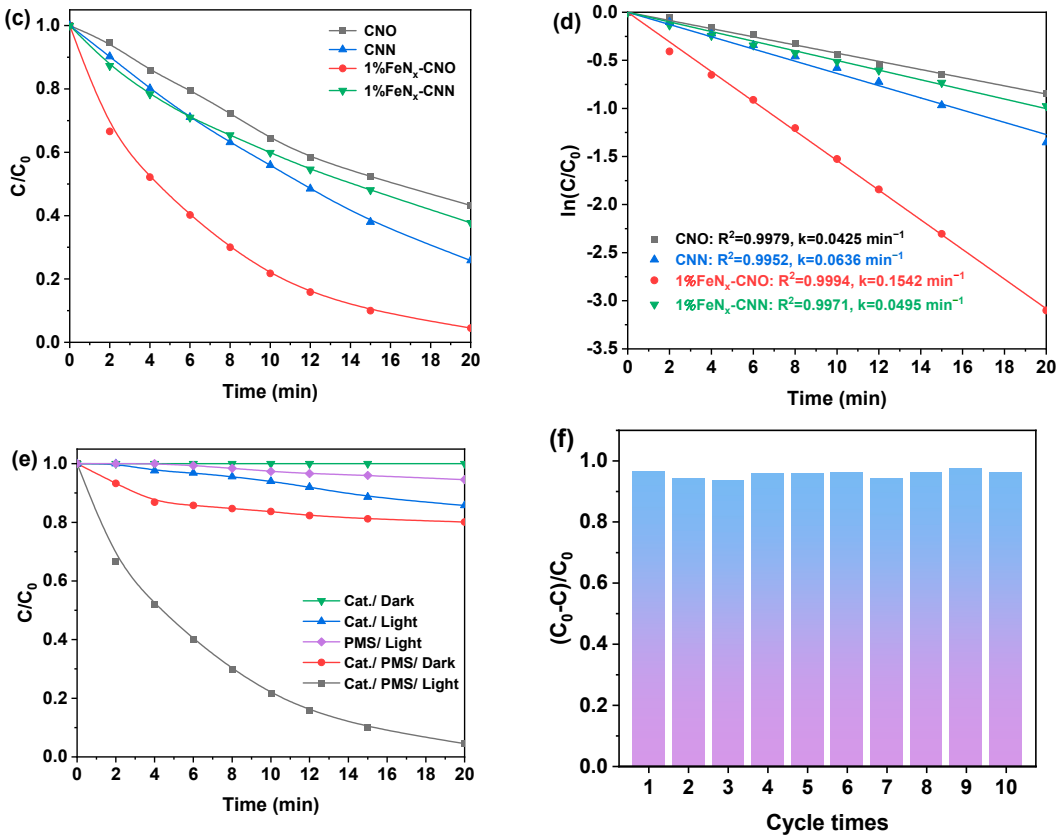

Figure 5. (**a**) Photocatalytic degradation of CBZ by n%FeN_x-CNO in PMS/light system and (**b**) their corresponding the pseudo-first-order kinetics; (**c**) photocatalytic degradation of CBZ by CNO, CNN, 1%FeN_x-CNO, and 1%FeN_x-CNN in PMS/light system and (**d**) their corresponding the pseudo-first-order kinetics; (**e**) the photocatalytic performance of 1%FeN_x-CNO under different reaction conditions; (**f**) consecutive recycling runs over 1%FeN_x-CNO. Conditions: [CBZ] = 2.5×10^{-5} M; [catalyst] = 0.1 g L^{-1}; [PMS] = 0.2 mM.

Figure 5e presents the catalytic performance of 1%FeN_x-CNO under different reaction conditions. Only about 5% of CBZ was removed within 20 min in the presence of PMS and light, suggesting that CBZ is difficult to degrade using PMS and light. Thus, the appropriate catalyst is crucial for the activation of PMS for the degradation of organic pollutants. In the absence of PMS, FeN_x-CNO has no ability to degrade CBZ in darkness, and the removal rate of CBZ can be up to 15% under light irradiation within 20 min. This indicates that FeN_x-CNO has low photocatalytic oxidation ability to degrade CBZ. By introducing PMS into the system and using 1%FeN_x-CNO as a catalyst, the removal rate of CBZ was significantly increased to 20% in darkness and 96% in light, respectively. These results demonstrate that FeN_x-CNO has efficient activation ability of PMS and photocatalytic degradation performance for CBZ under simulated sunlight irradiation. The recyclability and stability of catalysts are important factors in the practical industrial application of catalysts. As displayed in Figure 5f, 1%FeN_x-CNO kept high activity and stability to degrade CBZ in the presence of PMS and light, and the removal rate of CBZ still reached 92% in the 10th cycling run, indicating that the 1%FeN_x-CNO catalyst had excellent recyclability.

The reaction parameters—including PMS dosage, pH in the reaction solution, and different anionic species—in the photocatalytic degradation of CBZ with 1%FeN_x-CNO as catalyst were also studied. Figure S6a shows that the photocatalytic activity gradually increased with increasing PMS dosage from 0 to 0.2 mM, and optimal activity was obtained at 0.2 mM. This was attributed to the fact that FeN_x-CNO could activate PMS to produce many active radicals with strong oxidation, and the higher PMS dosage facilitated the production of more active radicals to participate in the catalytic reaction. However, when

further raising the PMS dosage to 0.3 mM, the activity did not improve, so 0.2 mM PMS was chosen for the subsequent experiments. Figure S6b shows that the 1%FeN_x-CNO maintained a high reactive activity in the pH range of 3–9. Figure S6c shows the influence of various anionic species (Cl^-, NO_3^-, SO_4^{2-}, and $ClCH_2COO^-$) on the catalytic activity of 1%FeN_x-CNO. No obvious decrease in catalytic efficiency was observed in the FeN_x-CNO/PMS/light catalytic system with the presence of anionic species (Cl^-, NO_3^-, SO_4^{2-}, and $ClCH_2COO^-$). These results indicate that the FeN_x-CNO/PMS/light catalytic system has good adaptability in acidic, weakly alkaline conditions and solution containing different inorganic salts.

In order to further evaluate the photocatalytic deep oxidation activity of FeN_x-CN, the mineralization rates of CBZ in the CNO/PMS, FeN_x-CNO/PMS, and FeN_x-CNN/PMS photocatalytic systems were compared. As shown in Figure S7, the TOC removal rate of CBZ by CNO, FeN_x-CNO, and FeN_x-CNN reached 45.2%, 70.4%, and 60.6%, respectively. This proves that FeN_x-CNO has a stronger mineralization ability than CNO and FeN_x-CNN.

To study its chemical stability, the 1%FeN_x-CNO catalyst before and after the reaction was characterized by XRD and XPS. As shown in Figure 6a, no obvious change was observed in the XRD patterns of fresh and used 1%FeN_x-CNO, which implied that the structure of FeN_x-CNO was stable after the cyclic reaction. The XPS results further support the chemical stability of the 1%FeN_x-CNO catalyst. As shown in Figure 6b–d, the C 1s, N 1s, and Fe 2p peaks of the used sample were similar to those of the fresh sample, except that the atom ratio of Fe(III) in the total Fe atoms increased from 62.7% in the fresh sample to 65% in the used sample, which indicates the existence of reversible redox behaviors of Fe(III) and Fe(II) in the reaction. The above results indicate that 1%FeN_x-CNO has high catalytic activity and good stability for the PMS activation and photocatalytic oxidation of organic pollutants in water.

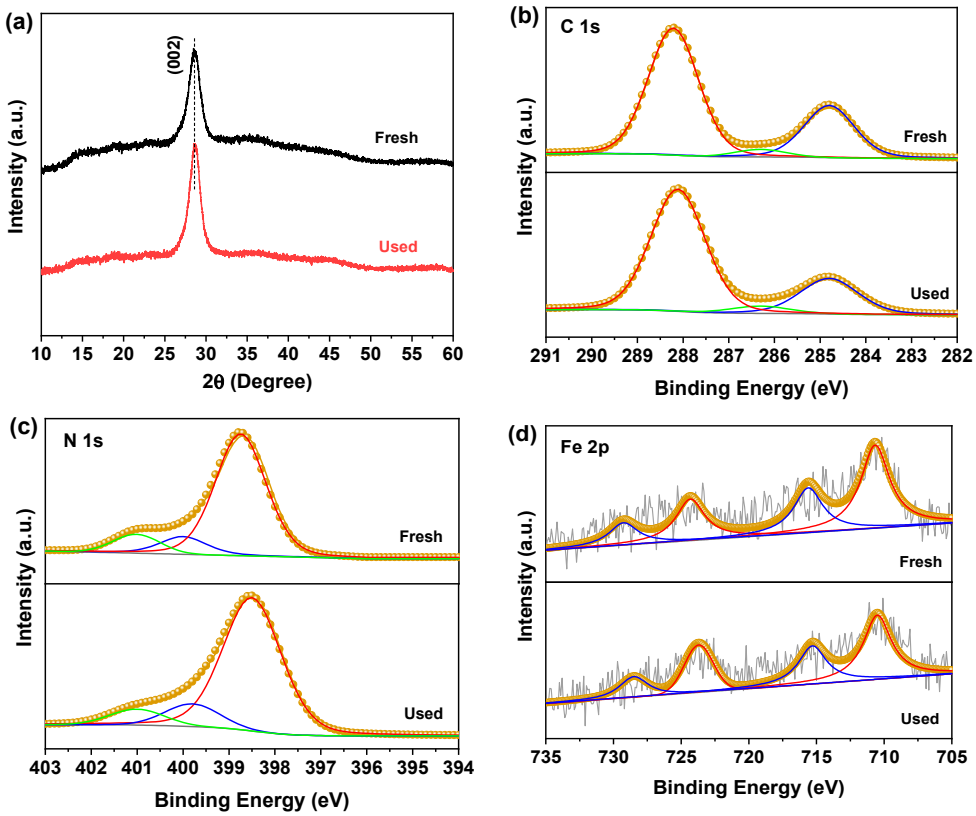

Figure 6. Comparison of XRD patterns (**a**) and high-resolution XPS spectra of (**b**) C 1s, (**c**) N 1s, and (**d**) Fe 2p of 1%FeN_x-CNO before and after recycle reaction.

2.4. Reaction Mechanism

In order to investigate the ROS generated in the CBZ degradation process with FeN_x-CNO catalyst, free radical quenching experiments were carried out by using a variety of trapping agents (including ethanol (EA), tert-butanol (TBA), *p*-benzoquinone (*p*-BQ), and L-Histidine (L-His)) [6]. Among them, EA can rapidly trap both •OH ($k = 1.2–2.8 \times 10^9\ M^{-1}\ s^{-1}$) and $SO_4\bullet^-$ ($k = 1.6–7.7 \times 10^9\ M^{-1}\ s^{-1}$). However, the reaction rate of TBA with •OH ($k = 3.8–7.6 \times 10^8\ M^{-1}\ s^{-1}$) was much faster than that of $SO_4\bullet^-$ ($k = 4.0–9.1 \times 10^5\ M^{-1}\ s^{-1}$) [58]. As can be seen in Figure 7a,b, in the FeN_x-CNO and FeN_x-CNN system, the CBZ degradation rate was suppressed partly by TBA, which indicates that •OH is one of the main active species for the photocatalytic process. The inhibition effect was enhanced when the same concentration of EA was added to the reaction system, suggesting that $SO_4\bullet^-$ also participated in the photocatalytic reaction. It is noteworthy that neither TBA nor EA completely inhibited the degradation in CBZ, so other active species were also formed in the photocatalytic system. Since *p*-BQ and L-His can react with $O_2\bullet^-$ ($k = 0.9–1.0 \times 10^9\ M^{-1}\ s^{-1}$) and $^1O_2$ ($k = 3.2 \times 10^7\ M^{-1}\ s^{-1}$), *p*-BQ or L-His was added to the reaction system to trap $O_2\bullet^-$ and $^1O_2$, respectively [58,59]. The presence of *p*-BQ or L-His significantly inhibited the photocatalytic activity to degrade CBZ, suggesting that a large amount of $O_2\bullet^-$ and $^1O_2$ was generated, and played a major role in the photocatalytic process. Figure S8 compares the inhibition rates of FeN_x-CNO and FeN_x-CNN for thew photocatalytic degradation of CBZ with different quenching agents. The FeN_x-CNO photocatalytic system was more capable of inhibiting CBZ degradation in the quenching experiments; that is, more active species were produced in this system than in the FeN_x-CNN photocatalytic system, which explained the higher photocatalytic activity of FeN_x-CNO catalysts than that of FeN_x-CNN.

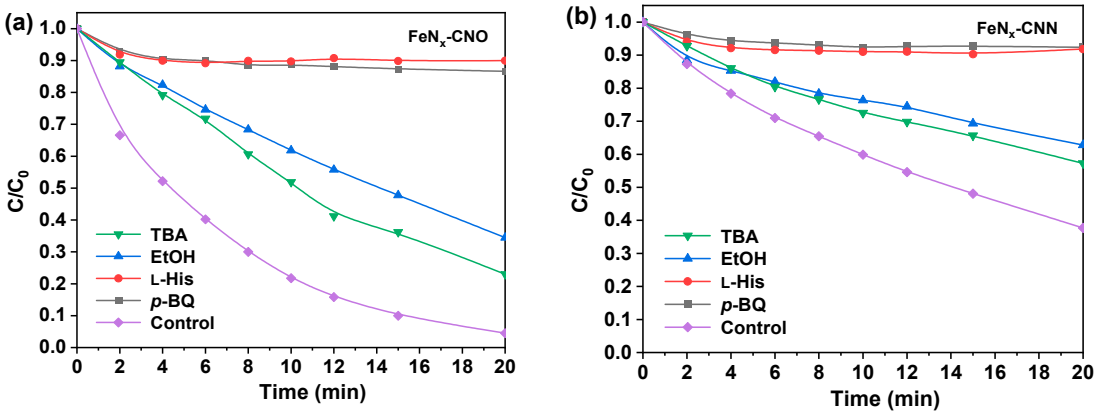

Figure 7. Effects of different trapping agents on the photocatalytic degradation efficiency of CBZ by (**a**) FeN_x-CNO and (**b**) FeN_x-CNN. [CBZ] = 2.5×10^{-5} M; [FeN_x-CNO] = [FeN_x-CNN] = 0.1 g L^{-1}; [PMS] = 0.2 mM; [EA] = [TBA]= 10 mM; [*p*-BQ] = [L-His]= 1 mM.

The possible formation of ROS in the photocatalytic degradation process was further analyzed using the EPR spin trapping method. As shown in Figure 8a, the quadruplet DMPO-•OH peaks with intensity ratios of 1:2:2:1 can be observed in the EPR spectra [59,60], and the peak intensities of FeN_x-CNO are much stronger than those of FeN_x-CNN and CNO. Six typical DMPO-$SO_4\bullet^-$ signal peaks with intensity ratios of 1:1:1:1:1:1 were also found in the spectra of FeN_x-CNO, and the peak intensities were also much stronger than those of FeN_x-CNN and CNO. These results support that FeN_x-CNO can promote the generation of more •OH and $SO_4\bullet^-$ during the photocatalytic process. As can be seen from Figure 8b,c, the characteristic signal peaks of DMPO-$O_2\bullet^-$ and TEMP-$^1O_2$ were all detected in the FeN_x-CNO, FeN_x-CNN and CNO. The peak intensities of DMPO-$O_2\bullet^-$ were in the order of FeN_x-CNO > g-C_3N_4 > FeN_x-CNN, while the TEMP-$^1O_2$ peak intensity of FeN_x-CNO is slightly stronger than that of FeN_x-CNN, and as much as five times that of CNO. The above results demonstrated that •OH, $SO_4\bullet^-$, $O_2\bullet^-$ and $^1O_2$ were the main active species in the photocatalytic reaction of FeN_x-CNO and explained the reason for

the higher photocatalytic degradation ability of FeN_x-CNO compared to FeN_x-CNN. The stronger peaks of FeN_x-CNO and FeN_x-CNN than those of pure g-C_3N_4 indicated that the formation of Fe-N_x bonds could promote the activation of PMS and the effective separation of photogenerated electron–hole pairs, thus generating more ROS to participate in the degradation process of CBZ.

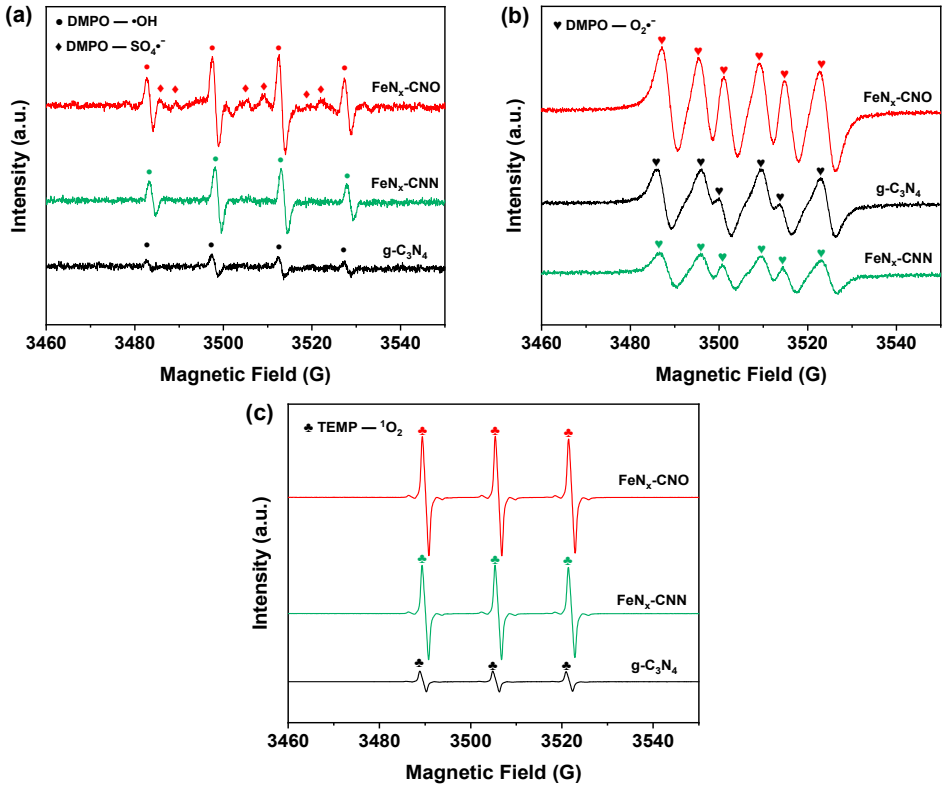

Figure 8. (**a**) DMPO spin-trapping EPR spectra in aqueous solution; (**b**) DMPO spin-trapping EPR spectra in methanol solution; and (**c**) TEMP spin-trapping EPR spectra in aqueous solution in the presence of g-C_3N_4, FeN_x-CNO, and FeN_x-CNN under simulated sunlight irradiation. [DMPO] = [TEMP] = 0.25 mM; [PMS] = 0.2 mM.

On the basis of the above discussion, a possible mechanism for the degradation of CBZ by FeN_x-CNO in the presence of PMS was proposed, and the schematic illustration is shown in Scheme 2. When FeN_x-CNO is illuminated by light, the electrons are excited to conduction band, and a pair of charge carriers are generated on the surface of catalyst (Equation (1)). As the more positive reduction potential of $O_2/O_2\bullet^-$ (−0.33 eV) than CB potential (−0.61 eV), the photogenerated electrons can be captured by dissolved oxygen in the water to generate $O_2\bullet^-$ radicals (Equation (2)). The photogenerated holes possess a strong oxidizing ability, which can be directly involved in the degradation reaction. As the more positive VB potential (2.17 eV) compared to the water oxidation potential of $OH^-/\bullet OH$ (1.99 eV), the holes can oxidize H_2O to produce ·OH (Equation (3)). The formation of the Fe-N_x bonds provides active sites for PMS activation, allowing for the oxidation of HSO_5^- by Fe(III) to form $SO_5\bullet^-$, while the latter is reduced to Fe(II). In addition, Fe(II) can further reduce HSO_5^- to form $SO_4\bullet^-$, while it is oxidized to Fe(III) (Equations (4) and (5)). The redox cycle of Fe(III) and Fe(II) species ensures the generation of massive $SO_5\bullet^-$ and $SO_4\bullet^-$. Meanwhile, $O_2\bullet^-$ or $SO_5\bullet^-$ can further react with H_2O molecules to generate $^1O_2$ (Equations (6,7)). The •OH in the system also comes from the oxidation of OH^- in the aqueous phase by $SO_4\bullet^-$ (Equation (8)). In summary, h^+, •OH,

$SO_4\bullet^-$, $O_2\bullet^-$, and $^1O_2$ all play a major role in the degradation of CBZ by the activation of PMS with FeN_x-CNO and light (Equation (9)).

$$FeN_x - CNO + hv \rightarrow e^- + h^+ \quad (1)$$

$$O_2 + e^- \rightarrow O_2^{\bullet -} \quad (2)$$

$$h^+ + H_2O \rightarrow \cdot OH + H^+ \quad (3)$$

$$Fe(\text{III}) + HSO_5^- \rightarrow Fe(\text{II}) + SO_5^{\bullet -} + H^+ \quad (4)$$

$$Fe(\text{II}) + HSO_5^{\bullet -} \rightarrow Fe(\text{III}) + SO_4^{\bullet -} + OH^- \quad (5)$$

$$O_2^{\bullet -} + \cdot OH \rightarrow {}^1O_2 + OH^- \quad (6)$$

$$SO_5^{\bullet -} + H_2O \rightarrow {}^1O_2 + HSO_4^- \quad (7)$$

$$SO_4^{\bullet -} + H_2O \rightarrow HSO_4^- + \cdot OH \quad (8)$$

$$CBZ + O_2^{\bullet -}/{}^1O_2/h^+/SO_4^{\bullet -}/\cdot OH \rightarrow \text{intermediates} \rightarrow CO_2 + H_2O \quad (9)$$

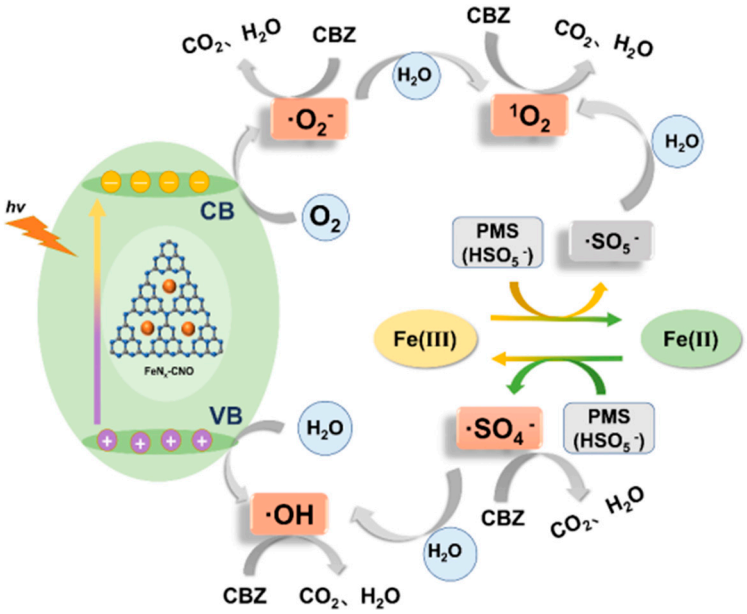

Scheme 2. Schematic illustration of the photocatalytic degradation mechanism of CBZ by FeN_x-CNO/PMS/light system.

2.5. CBZ Degradation Pathway

UPLC/HDMS in positive ion mode was used to detect the intermediates generated during the degradation of CBZ by FeN_x-CNO in the presence of PMS. The detected intermediate products are summarized in Table S5. Figure 9 displays a possible pathway for the degradation of CBZ by FeN_x-CNO. After the activation of PMS by FeN_x-CNO, a large amount of ROS was generated to attack olefinic double bonds with high frontier electron density (FED) on the central heterocycle of the CBZ molecule, which were easy to dehydrogenate and hydroxylate to form intermediate A (m/z = 267.0770) and B (m/z = 253.0977), respectively. The splitting C-C bonds in the central ring of compound A and ring opening of the epoxidation product B produced intermediate C (m/z = 269.0926). The epoxidation product B was also oxidized by ROS to generate intermediate D (m/z = 251.0816). In addition, the amide group (–$CONH_2$) in intermediate B was firstly deamidated and rearranged to form intermediates E (m/z = 224.0712) and F (m/z =2 08.0762). Then, intermediates E and F could be further oxidized to eliminate the carbonyl and aldehyde groups to yield G (m/z = 196.0762) and H (m/z = 180.0815). The toxicity of the main intermediates in the

degradation process was less than that of CBZ. These intermediates were finally degraded completely by ROS to produce CO_2 and H_2O [60].

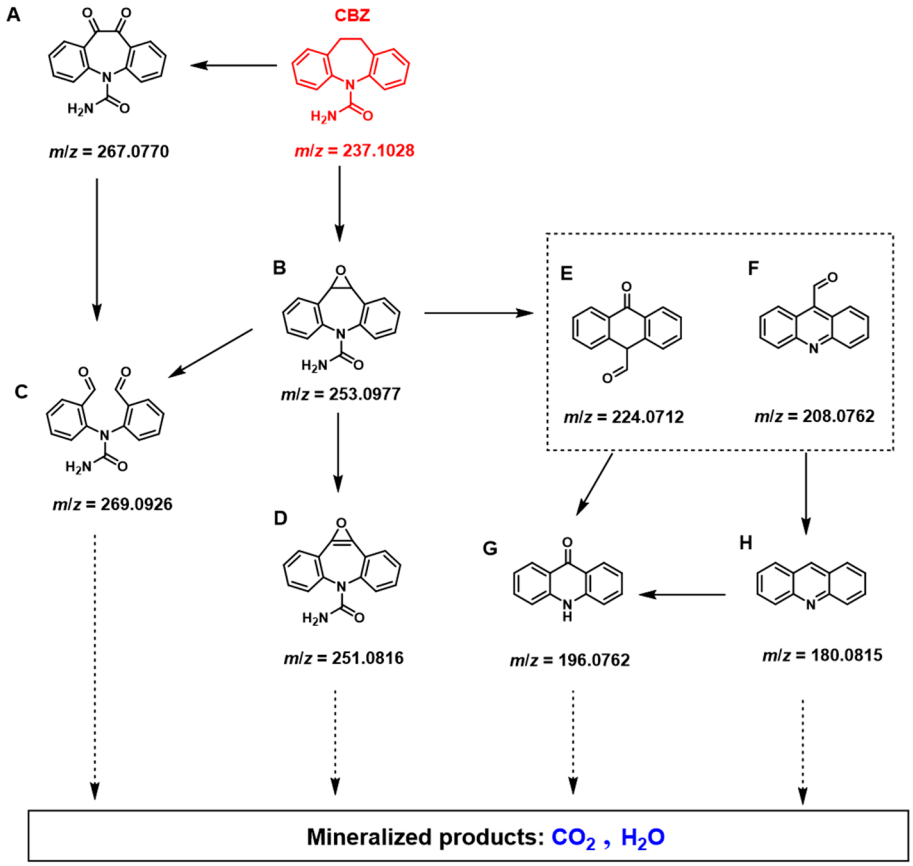

Figure 9. A possible pathway for the degradation of CBZ by FeN_x-CNO/PMS under simulated sunlight.

3. Conclusions

In this work, Fe-doped carbon nitride was prepared by one-step thermal polymerization of urea and $Fe(NO_3)_3$. The effect of polymerization atmosphere, including static air and N_2, on the structure and optical and photocatalytic properties were studied in detail. The results showed that Fe is probably doped into the carbon nitride structure in the form of Fe-N_x bonds in both FeN_x-CNO and FeN_x-CNN samples. FeN_x-CNO contains more oxygen vacancies than FeN_x-CNN. Moreover, thermal polymerization in air promoted the disruption of carbon nitride and the formation of more pore structure, leading to a significant increase in the specific surface area. As a result, 1%FeN_x-CNO showed higher photocatalytic activity in the CBZ degradation than CNO and FeN_x-CNN. The degradation efficiency could still reach 93% after 10 cycles of reaction. The reactive species $SO_4\bullet^-$, $\bullet OH$, $O_2\bullet^-$, and $^1O_2$ played a major role in the oxidation of CBZ in the photocatalytic systems. Compared to the FeN_x-CNN/PMS system, more reactive species were produced in the FeN_x-CNO/PMS system. A possible pathway for the degradation of CBZ by FeN_x-CNO/PMS was studied by the detecting intermediates by UPLC-HDMS. This study offers an efficient Fe-based catalyst for the treatment of pharmaceutical pollutants in water.

Supplementary Materials: The following supporting information can be downloaded at https://www.mdpi.com/article/10.3390/catal14080520/s1, Experimental section: materials, synthesis of Fe-doped g-C_3N_4 catalyst, characterization and photocatalytic tests; Figure S1: XRD patterns and FT-IR spectra of n%FeN_x-CN, Figure S2: SEM images, Figure S3: TEM images of g-C_3N_4, Figure S4: Nitrogen adsorption-desorption isotherms and pore size distributions, Figure S5: XPS Full Spectrum, Figure S6: the photocatalytic activity of 1%FeN_x-CNO under different PMS concentrations, different pH conditions, and different inorganic salt ions, Figure S7: TOC removal rate, Figure S8: comparison

of inhibition rates of FeN_x-CNO and FeN_x-CNN by different trapping agents, Table S1: BET surface areas, pore volumes, and pore average diameter, Table S2: proportion of different chemical bonds about C atoms, Table S3: proportion of different chemical bonds about O atoms in different samples, Table S4: Comparison of photocatalytic performance of various catalysts for CBZ degradation in the presence of PMS, Table S5: The intermediate products formed during the degradation of CBZ by FeN_x-CNO/PMS/Light system were detected by UPLC/HDMS in positive ion mode; [61–69].

Author Contributions: X.P., R.P. and L.C. were responsible for original draft preparation, investigation, and validation. X.C. was responsible for review, editing, and funding acquisition. F.C. and W.L. were responsible for data curation and validation. All authors have read and agreed to the published version of the manuscript.

Funding: This research was funded by the Baima Lake Laboratory Joint Funds of the Zhejiang Provincial Natural Science Foundation of China (LBMHY24E060003), the Scientific Research Foundation of Zhejiang Sci-Tech University (19212450-Y), and the Fundamental Research Funds of Zhejiang Sci-Tech University (23212112-Y).

Data Availability Statement: The authors can confirm that all relevant data are included in the article.

Conflicts of Interest: The authors do not have any financial or non-financial interests that are directly or indirectly related to the work submitted for publication.

References

1. Xu, P.; Zhang, R.; Gong, J.; Luo, Y.; Zhuang, Y.; Zhang, P. S-Scheme $WO_3/SnIn_4S_8$ Heterojunction for Water Purification: Enhanced Photocatalytic Performance and Mechanism. *Catalysts* **2023**, *13*, 1450. [CrossRef]
2. Guo, H.; Li, Z.; Xiang, L.; Jiang, N.; Zhang, Y.; Wang, H.; Li, J. Efficient Removal of Antibiotic Thiamphenicol by Pulsed Discharge Plasma Coupled with Complex Catalysis Using Graphene-WO_3-Fe_3O_4 Nanocomposites. *J. Hazard. Mater.* **2021**, *403*, 123673. [CrossRef]
3. Stella, R.; Sreevani, I.; Gurugubelli, T.; Ravikumar, R.; Koutavarapu, R. Enhanced Solar Light-Driven Photocatalytic Degradation of Tetracycline Using Fe^{3+}-Doped CdO/ZnS Nanocomposite: Mechanistic Insights and Performance Evaluation. *Catalysts* **2023**, *13*, 1312. [CrossRef]
4. Goudarzy, F.; Zolgharnein, J.; Ghasemi, J.B. Determination and Degradation of Carbamazepine Using g-C_3N_4@CuS Nanocomposite as Sensitive Fluorescence Sensor and Efficient Photocatalyst. *Inorg. Chem. Commun.* **2022**, *141*, 109512. [CrossRef]
5. Yang, Y.; Ok, Y.S.; Kim, K.-H.; Kwon, E.E.; Tsang, Y.F. Occurrences and Removal of Pharmaceuticals and Personal Care Products (PPCPs) in Drinking Water and Water/Sewage Treatment Plants: A Review. *Sci. Total Environ.* **2017**, *596–597*, 303–320. [CrossRef] [PubMed]
6. Cheng, L.; Sun, S.; Chen, X.; Chen, F.; Chen, X.; Lu, W. Convenient Fabrication of Ultrafine VO_x Decorated on Porous g-C_3N_4 for Boosting Photocatalytic Degradation of Pharmaceuticals with Peroxymonosulfate. *Surf. Interface* **2023**, *42*, 103300. [CrossRef]
7. Wu, D.; Sui, Q.; Yu, X.; Zhao, W.; Li, Q.; Fatta-Kassinos, D.; Lyu, S. Identification of Indicator PPCPs in Landfill Leachates and Livestock Wastewaters Using Multi-Residue Analysis of 70 PPCPs: Analytical Method Development and Application in Yangtze River Delta, China. *Sci. Total Environ.* **2021**, *753*, 141653. [CrossRef] [PubMed]
8. Xiong, Q.; Chen, Y.; Xu, T.; Zhu, Z.; Chen, W.; Lu, W. Highly Efficient Purification of Emerging Pollutants and Bacteria in Natural Water by g-C_3N_4-Sheltered Fibers Containing TiO_2. *Appl. Surf. Sci.* **2021**, *559*, 149839. [CrossRef]
9. Anjali, R.; Shanthakumar, S. Insights on the Current Status of Occurrence and Removal of Antibiotics in Wastewater by Advanced Oxidation Processes. *J. Environ. Manage.* **2019**, *246*, 51–62. [CrossRef]
10. Chen, J.; Hu, J.; Lin, Y.; Liu, X.; Liang, J.; Zhang, K.; Jiang, B.; Luo, H.; Li, L.; An, X.; et al. Visible Light-Driven Cl-g-C_3N_4 Activated Peroxydisulfate Process for TMP Efficient Degradation in a Wide pH Range. *J. Water Process Eng.* **2024**, *59*, 105056. [CrossRef]
11. Zhang, G.; Wu, Z.; Liu, H.; Ji, Q.; Qu, J.; Li, J. Photoactuation Healing of α-FeOOH@g-C_3N_4 Catalyst for Efficient and Stable Activation of Persulfate. *Small* **2017**, *13*, 1702225. [CrossRef] [PubMed]
12. Liu, Y.; Wang, X.; Sun, Q.; Chen, L.; Yuan, M.; Sun, Z.; Zhang, Y.; Xia, S.; Zhao, J. Enhanced Activation of Peroxymonosulfate by a Floating Cu^0-MoS_2/C_3N_4 Photocatalyst under Visible-Light Assistance for Tetracyclines Degradation and *Escherichia Coli* Inactivation. *Chem. Eng. J.* **2023**, *457*, 141220. [CrossRef]
13. Zhang, J.; Zhao, X.; Wang, Y.; Gong, Y.; Cao, D.; Qiao, M. Peroxymonosulfate-Enhanced Visible Light Photocatalytic Degradation of Bisphenol A by Perylene Imide-Modified g-C_3N_4. *Appl. Catal. B Environ.* **2018**, *237*, 976–985. [CrossRef]
14. Zhao, G.; Li, W.; Zhang, H.; Wang, W.; Ren, Y. Single Atom Fe-Dispersed Graphitic Carbon Nitride (g-C_3N_4) as a Highly Efficient Peroxymonosulfate Photocatalytic Activator for Sulfamethoxazole Degradation. *Chem. Eng. J.* **2022**, *430*, 132937. [CrossRef]
15. Chen, M.; Wang, N.; Zhu, L. Single-Atom Dispersed Co-N-C: A Novel Adsorption-Catalysis Bifunctional Material for Rapid Removing Bisphenol, A. *Catal. Today* **2020**, *348*, 187–193. [CrossRef]

16. Xie, Q.; Wang, C.; Shen, W.; Fu, Y.; Si, Y. Regulating Intermediate Concentration to Synthesize Highly Crystalline g-C_3N_4 under Spontaneous Ultrahigh Pressure. *ChemNanoMat* **2023**, e202300102. [CrossRef]
17. Zhang, L.; Liu, D.; Guan, J.; Chen, X.; Guo, X.; Zhao, F.; Hou, T.; Mu, X. Metal-free g-C_3N_4 Photocatalyst by Sulfuric Acid Activation for Selective Aerobic Oxidation of Benzyl Alcohol under Visible Light. *Mater. Res. Bull.* **2014**, *59*, 84–92. [CrossRef]
18. Zhen, J.; Sun, J.; Xu, X.; Wu, Z.; Song, W.; Ying, Y.; Liang, S.; Miao, L.; Cao, J.; Lv, W.; et al. M−N_3 Configuration on Boron Nitride Boosts Singlet Oxygen Generation via Peroxymonosulfate Activation for Selective Oxidation. *Angew Chem. Int. Ed.* **2024**, *63*, e202402669. [CrossRef]
19. Yanan, S.; Xing, X.; Yue, Q.; Gao, B.; Li, Y. Nitrogen-Doped Carbon Nanotubes Encapsulating Fe/Zn Nanoparticles as a Persulfate Activator for Sulfamethoxazole Degradation: Role of Encapsulated Bimetallic Nanoparticles and Nonradical Reaction. *Environ. Sci. Nano.* **2020**, *7*, 1444–1453. [CrossRef]
20. Wang, C.; Xie, Q.; Shen, W.; Chen, Z.; Hong, X.; Fu, Y.; Si, Y. Synthesis of Highly Crystallized g-C_3N_4 by Regulating Staged Gaseous Intermediates for Hydrogen Production. *J. Mater. Res.* **2023**, *38*, 3214–3226. [CrossRef]
21. Wang, L.; Rao, L.; Ran, M.; Ran, M.; Shentu, Q.; Wu, Z.; Song, W.; Zhang, Z.; Li, H.; Yao, Y.; et al. A Polymer Tethering Strategy to Achieve High Metal Loading on Catalysts for Fenton Reactions. *Nat. Commun.* **2023**, *14*, 7841. [CrossRef] [PubMed]
22. Kalidasan, K.; Mallapur, S.; Munirathnam, K.; Nagarajaiah, H.; Reddy, M.B.M.; Kakarla, R.R.; Raghu, A.V. Transition Metals-Doped g-C_3N_4 Nanostructures as Advanced Photocatalysts for Energy and Environmental Applications. *Chemosphere* **2024**, *352*, 141354. [CrossRef] [PubMed]
23. Chen, X.; Hu, R. DFT-Based Study of Single Transition Metal Atom Doped g-C_3N_4 as Alternative Oxygen Reduction Reaction Catalysts. *Int. J. Hydrogen Energ.* **2019**, *44*, 15409–15416. [CrossRef]
24. Lai, L.; Zhou, H.; Zhang, H.; Ao, Z.; Pan, Z.; Chen, Q.; Xiong, Z.; Yao, G.; Lai, B. Activation of Peroxydisulfate by Natural Titanomagnetite for Atrazine Removal via Free Radicals and High-Valent Iron-Oxo Species. *Chem. Eng. J.* **2020**, *387*, 124165. [CrossRef]
25. Wang, L.; Lu, W.; Ni, D.; Xu, T.; Li, N.; Zhu, Z.; Chen, H.; Chen, W. Solar-Initiated Photocatalytic Degradation of Carbamazepine on Excited-State Hexadecachlorophthalocyanine in the Presence of Peroxymonosulfate. *Chem. Eng. J.* **2017**, *330*, 625–634. [CrossRef]
26. Chen, X.; Cheng, L.; Yang, Y.; Chen, X.; Chen, F.; Lu, W. Construction of High-Density Fe Clusters Embedded in a Porous Carbon Nitride Catalyst with Effectively Selective Transformation of Benzene. *ACS Sustain. Chem. Eng.* **2023**, *11*, 1518–1526. [CrossRef]
27. Tang, W.; Tian, Y.; Chen, B.; Xu, Y.; Li, B.; Jing, X.; Zhang, J.; Xu, S. Supramolecular Copolymerization Strategy for Realizing the Broadband White Light Luminescence Based on N-Deficient Porous Graphitic Carbon Nitride (g-C_3N_4). *ACS Appl. Mater. Interfaces* **2020**, *12*, 6396–6406. [CrossRef]
28. Shentu, Q.; Wu, Z.; Song, W.; Pan, S.; Zhou, Z.; Lv, W.; Song, C.; Yao, Y. Carbon Doped Boron Nitride Nanosheet as Efficient Metal-Free Catalyst for Peroxymonosulfate Activation: Important Role of B-N-C Moieties. *Chem. Eng. J.* **2022**, *446*, 137274. [CrossRef]
29. Zhao, Z.; Zhou, M.; Li, N.; Yao, Y.; Chen, W.; Lu, W. Degradation of Carbamazepine by MWCNTs-Promoted Generation of High-Valent Iron-Oxo Species in a Mild System with O-Bridged Iron Perfluorophthalocyanine Dimers. *J. Environ. Sci.* **2021**, *99*, 260–266. [CrossRef]
30. Yang, F.; Yin, C.; Zhang, M.; Zhu, J.; Ai, X.; Shi, W.; Peng, G. Enhanced Fe(III)/Fe(II) Redox Cycle for Persulfate Activation by Reducing Sulfur Species. *Catalysts* **2022**, *12*, 1435. [CrossRef]
31. Chen, S.; Lu, W.; Shen, H.; Xu, S.; Chen, X.; Xu, T.; Wang, Y.; Chen, Y.; Gu, Y.; Wang, C.; et al. The Development of New Pigments: Colorful g-C_3N_4-Based Catalysts for Nicotine Removal. *Appl. Catal. B Environ.* **2019**, *254*, 500–509. [CrossRef]
32. Usman, M.; Zeb, Z.; Ullah, H.; Suliman, M.H.; Humayun, M.; Ullah, L.; Shah, S.N.A.; Ahmed, U.; Saeed, M. A Review of Metal-Organic Frameworks/Graphitic Carbon Nitride Composites for Solar-Driven Green H_2 Production, CO_2 Reduction, and Water Purification. *J. Environ. Chem. Eng.* **2022**, *10*, 107548. [CrossRef]
33. Martin, D.J.; Qiu, K.; Shevlin, S.A.; Handoko, A.D.; Chen, X.; Guo, Z.; Tang, J. Highly Efficient Photocatalytic H_2 Evolution from Water Using Visible Light and Structure-Controlled Graphitic Carbon Nitride. *Angew. Chem. Int. Ed.* **2014**, *53*, 9240–9245. [CrossRef] [PubMed]
34. Song, X.; Yang, Q.; Jiang, X.; Yin, M.; Zhou, L. Porous Graphitic Carbon Nitride Nanosheets Prepared under Self-Producing Atmosphere for Highly Improved Photocatalytic Activity. *Appl. Catal. B Environ.* **2017**, *217*, 322–330. [CrossRef]
35. Jiménez-Calvo, P.; Marchal, C.; Cottineau, T.; Caps, V.; Keller, V. Influence of the Gas Atmosphere during the Synthesis of g-C_3N_4 for Enhanced Photocatalytic H_2 Production from Water on Au/g-C_3N_4 Composites. *J. Mater. Chem. A* **2019**, *7*, 14849–14863. [CrossRef]
36. Guo, W.; Zhang, J.; Li, G.; Xu, C. Enhanced Photocatalytic Activity of P-Type (K, Fe) Co-Doped g-C_3N_4 Synthesized in Self-Generated NH_3 Atmosphere. *Appl. Surf. Sci.* **2019**, *470*, 99–106. [CrossRef]
37. Chen, X.; Zhang, J.; Fu, X.; Antonietti, M.; Wang, X. Fe-g-C_3N_4-Catalyzed Oxidation of Benzene to Phenol Using Hydrogen Peroxide and Visible Light. *J. Am. Chem. Soc.* **2009**, *131*, 11658–11659. [CrossRef] [PubMed]
38. Gao, Y.; Zhu, Y.; Lyu, L.; Zeng, Q.; Xing, X.; Hu, C. Electronic Structure Modulation of Graphitic Carbon Nitride by Oxygen Doping for Enhanced Catalytic Degradation of Organic Pollutants through Peroxymonosulfate Activation. *Environ. Sci. Technol.* **2018**, *52*, 14371–14380. [CrossRef] [PubMed]

39. Yan, W.; Yan, L.; Jing, C. Impact of Doped Metals on Urea-Derived g-C_3N_4 for Photocatalytic Degradation of Antibiotics: Structure, Photoactivity and Degradation Mechanisms. *Appl. Catal. B Environ.* **2019**, *244*, 475–485. [CrossRef]
40. Zhang, S.; Gao, H.; Huang, Y.; Wang, X.; Hayat, T.; Li, J.; Xu, X.; Wang, X. Ultrathin g-C_3N_4 Nanosheets Coupled with Amorphous Cu-Doped FeOOH Nanoclusters as 2D/0D Heterogeneous Catalysts for Water Remediation. *Environ. Sci. Nano* **2018**, *5*, 1179–1190. [CrossRef]
41. Zhou, Y.; Zhang, L.; Wang, W. Direct Functionalization of Methane into Ethanol over Copper Modified Polymeric Carbon Nitride via Photocatalysis. *Nat. Commun.* **2019**, *10*, 506. [CrossRef]
42. Zang, Y.N.; Yang, S.S.; Ding, J.; Zhao, S.Y.; Chen, C.X.; He, L.; Ren, N.Q. A Biochar-Promoted V_2O_5/g-C_3N_4 Z-Scheme Heterostructure for Enhanced Simulated Solar Light-Driven Photocatalytic Activity. *RSC Adv.* **2021**, *11*, 15106–15117. [CrossRef] [PubMed]
43. Wu, X.; Xie, W.; Liu, X.; Liu, X.; Zhao, Q. Two-Dimensional Fe-N-C Nanosheets for Efficient Oxygen Reduction Reaction. *Catalysts* **2022**, *12*, 1276. [CrossRef]
44. Ma, D.; Wu, J.; Gao, M.; Xin, Y.; Ma, T.; Sun, Y. Fabrication of Z-Scheme g-C_3N_4/RGO/Bi_2WO_6 Photocatalyst with Enhanced Visible-Light Photocatalytic Activity. *Chem. Eng. J.* **2016**, *290*, 136–146. [CrossRef]
45. Sun, L.; Yang, M.; Huang, J.; Yu, D.; Hong, W.; Chen, X. Freestanding Graphitic Carbon Nitride Photonic Crystals for Enhanced Photocatalysis. *Adv. Funct. Mater.* **2016**, *26*, 4943–4950. [CrossRef]
46. Li, W.; Wu, X.; Li, S.; Tang, W.; Chen, Y. Magnetic Porous Fe_3O_4/Carbon Octahedra Derived from Iron-Based Metal-Organic Framework as Heterogeneous Fenton-like Catalyst. *Appl. Surf. Sci.* **2018**, *436*, 252–262. [CrossRef]
47. Hu, J.; Zhang, P.; An, W.; Liu, L.; Liang, Y.; Cui, W. In-Situ Fe-Doped g-C_3N_4 Heterogeneous Catalyst via Photocatalysis-Fenton Reaction with Enriched Photocatalytic Performance for Removal of Complex Wastewater. *Appl. Catal. B Environ.* **2019**, *245*, 130–142. [CrossRef]
48. Cheng, X.; Wang, J.; Zhao, K.; Bi, Y. Spatially Confined Iron Single-Atom and Potassium Ion in Carbon Nitride toward Efficient CO_2 Reduction. *Appl. Catal. B Environ.* **2022**, *316*, 121643. [CrossRef]
49. Chen, X.; Xiao, Q.; Yang, Y.; Dong, B.; Zhao, Z. Constructing Polyphosphazene Microsphere-Supported Pd Nanocatalysts for Efficient Hydrogenation of Quinolines under Mild Conditions. *Catalysts* **2024**, *14*, 345. [CrossRef]
50. Peng, X.; Wu, J.; Zhao, Z.; Wang, X.; Dai, H.; Xu, L.; Xu, G.; Jian, Y.; Hu, F. Activation of Peroxymonosulfate by Single-Atom Fe-g-C_3N_4 Catalysts for High Efficiency Degradation of Tetracycline via Nonradical Pathways: Role of High-Valent Iron-Oxo Species and Fe–N_x Sites. *Chem. Eng. J.* **2022**, *427*, 130803. [CrossRef]
51. Ding, C.; Kang, S.; Li, W.; Gao, W.; Zhang, Z.; Zheng, L.; Cui, L. Mesoporous Structure and Amorphous Fe-N Sites Regulation in Fe-g-C_3N_4 for Boosted Visible-Light-Driven Photo-Fenton Reaction. *J. Ind. Eng. Chem.* **2022**, *608*, 2515–2528. [CrossRef] [PubMed]
52. Salazar-Aguilar, A.D.; Vega, G.; Casas, J.A.; Vega-Díaz, S.M.; Tristan, F.; Meneses-Rodríguez, D.; Belmonte, M.; Quintanilla, A. Direct Hydroxylation of Phenol to Dihydroxybenzenes by H_2O_2 and Fe-based Metal-Organic Framework Catalyst at Room Temperature. *Catalysts* **2020**, *10*, 172. [CrossRef]
53. Xue, B.; Chen, Y.; Hong, Y.; Ma, D.-Y.; Xu, J.; Li, Y.-X. Facile Synthesis of Fe-Containing Graphitic Carbon Nitride Materials and Their Catalytic Application in Direct Hydroxylation of Benzene to Phenol. *Chin. J. Catal.* **2018**, *39*, 1263–1271. [CrossRef]
54. Cirena, Z.; Nie, Y.; Li, Y.; Hu, H.; Huang, X.; Tan, X.; Yu, T. Fe Doped g-C_3N_4 Composited $ZnIn_2S_4$ Promoting Cr(VI) Photoreduction. *Chin. Chem. Lett.* **2023**, *34*, 107726. [CrossRef]
55. Liu, G.; Dong, G.; Zeng, Y.; Wang, C. The Photocatalytic Performance and Active Sites of g-C_3N_4 Effected by the Coordination Doping of Fe(III). *Chin. J. Catal.* **2020**, *41*, 1564–1572. [CrossRef]
56. An, D.S.; Zeng, H.Y.; Xiao, G.F.; Xiong, J.; Chen, C.R.; Hu, G. Cr(VI) Reduction over Ag_3PO_4/g-C_3N_4 Composite with p-n Heterostructure under Visible-Light Irradiation. *J. Taiwan Inst. Chem. Eng.* **2020**, *117*, 133–143. [CrossRef]
57. Hou, J.; Yang, C.; Wang, Z.; Zhou, W.; Jiao, S.; Zhu, H. In Situ Synthesis of α–β Phase Heterojunction on Bi_2O_3 Nanowires with Exceptional Visible-Light Photocatalytic Performance. *Appl. Catal. B Environ.* **2013**, *142–143*, 504–511. [CrossRef]
58. Fang, G.; Gao, J.; Dionysiou, D.D.; Liu, C.; Zhou, D. Activation of Persulfate by Quinones: Free Radical Reactions and Implication for the Degradation of PCBs. *Environ. Sci. Technol.* **2013**, *47*, 4605–4611. [CrossRef] [PubMed]
59. Elena, A.; Rachele, O.; Douglas, E.L.; Paul, R.E.; Kristopher, M. Aqueous Singlet Oxygen Reaction Kinetics of Furfuryl Alcohol: Effect of Temperature, pH, and Salt Content. *Environ. Sci. Processes Impacts* **2017**, *19*, 507–516.
60. Shen, Z.; Fan, L.; Yang, S.; Yao, Y.; Chen, H.; Wang, W. Fe-based Carbonitride as Fenton-like Catalyst for the Elimination of Organic Contaminants. *Environ. Res.* **2021**, *198*, 110486. [CrossRef]
61. Mei, X.; Chen, S.; Wang, G.; Chen, W.; Lu, W.; Zhang, B.; Fang, Y.; Qi, C. Metal-free Carboxyl Modified g-C_3N_4 for Enhancing Photocatalytic Degradation Activity of Organic Pollutants Through Peroxymonosulfate Activation in Wastewater under Solar Radiation. *J. Solid State Chem.* **2022**, *310*, 123053. [CrossRef]
62. Qi, Y.; Zhou, X.; Li, Z.; Yin, R.; Qin, J.; Li, H.; Guo, W.; Li, A.; Qiu, R. Photo-Induced Holes Initiating Peroxymonosulfate Oxidation for Carbamazepine Degradation via Singlet Oxygen. *Catalysts* **2022**, *12*, 1327. [CrossRef]
63. Dong, L.; Xu, T.; Chen, W.; Lu, W. Synergistic Multiple Active Species for the Photocatalytic Degradation of Contaminants by Imidazole-Modified g-C_3N_4 Coordination with Iron Phthalocyanine in the Presence of Peroxymonosulfate. *Chem. Eng. J.* **2019**, *357*, 198–208. [CrossRef]

64. Li, J.; Huang, W.; Yang, L.; Gou, G.; Zhou, C.; Li, L.; Li, N.; Liu, C.; Lai, B. Novel Ag_3PO_4 Modified Tubular Carbon Nitride with Visible-light-driven Peroxymonosulfate Activation: A Wide pH Tolerance and Reaction Mechanism. *Chem. Eng. J.* **2022**, *432*, 133588. [CrossRef]
65. Tao, Y.; Fan, G.; Li, X.; Cao, X.; Du, B.; Li, H.; Luo, J.; Hong, Z.; Xu, Q. Recyclable Magnetic AgBr/BiOBr/Fe_3O_4 Photocatalytic Activation Peroxymonosulfate for Carbamazepine Degradation: Synergistic Effect and Mechanism. *Ser. Purif. Technol.* **2024**, *330*, 125392. [CrossRef]
66. Zhang, Y.; Cheng, Y.; Qi, H. Synergistic Degradation of Organic Pollutants on $CoFe_2O_4$/rGO Nanocomposites by Peroxymonsulfate Activation under LED Irradiation. *Appl. Surf. Sci.* **2022**, *579*, 152151. [CrossRef]
67. Wu, F.; Huang, H.; Xu, T.; Lu, W.; Li, N.; Chen, W. Visible-Light-Assisted Peroxymonosulfate Activation and Mechanism for the Degradation of Pharmaceuticals over Pyridyl-Functionalized Graphitic Carbon Nitride Coordinated with Iron Phthalocyanine. *Appl. Catal. B Environ.* **2017**, *218*, 230–239. [CrossRef]
68. Zeng, T.; Li, S.; Shen, Y.; Zhang, H.; Feng, H.; Zhang, X.; Li, L.; Cai, Z.; Song, S. Sodium Doping and 3D Honeycomb Nanoarchitecture: Key Features of Covalent Triazine-based Frameworks (CTF) Organocatalyst for Enhanced Solar-driven Advanced Oxidation Processes. *Appl. Catal. B Environ.* **2019**, *257*, 117915. [CrossRef]
69. Yang, L.; Jia, Y.; Peng, Y.; Zhou, P.; Yu, D.; Zhao, C.; He, J.; Zhan, C.; Lai, B. Visible-light Induced Activation of Persulfate by Self-assembled EHPDI/TiO_2 Photocatalyst toward Efficient Degradation of Carbamazepine. *Sci. Total Environ.* **2021**, *783*, 146996. [CrossRef]